Published in final edited form as:
J Am Chem Soc. 2011 July 27; 133(29): 11270–11278. doi:10.1021/ja202836s.

Role of Fe doping in tuning the band gap of TiO_2 for photo-oxidation induced cytotoxicity paradigm

Saji George[ς,δ,+], **Suman Pokhrel**[¥,+], **Zhaoxia Ji**[χ], **Bryana L. Henderson**[χ], **Tian Xia**[ς,δ], **LinJiang Li**[ς,δ], **Jeffrey I. Zink**[χ], **André E. Nel**[ς,δ], and **Lutz Mädler**[¥,δ,*]

[¥]Foundation Institute of Materials Science (IWT), Department of Production Engineering, University of Bremen, Germany

[ς]Department of Medicine-Division of NanoMedicine, University of California, Los Angeles, California, USA

[δ]California NanoSystems Institute at University of California, Los Angeles, California, USA

[χ]Department of Chemistry and Biochemistry, University of California, Los Angeles, California, USA

Abstract

UV-Light induced electron-hole (e^-/h^+) pair generation and free radical production in TiO_2 based nanoparticles is a major conceptual paradigm for biological injury. However, to date, this hypothesis has been difficult to experimentally verify due to the high energy of UV light that is intrinsically highly toxic to biological systems. Here, a versatile flame spray pyrolysis (FSP) synthetic process has been exploited to synthesize a library of iron doped (0–10 at wt%) TiO_2 nanoparticles. These particles have been tested for photoactivation-mediated cytotoxicity using near-visible light exposure. The reduction in TiO_2 band gap energy with incremental levels of Fe loading maintained the nanoparticle crystalline structure in spite of homogeneous Fe distribution (demonstrated by XRD, HRTEM, SAED, EFTEM, and EELS). Photochemical studies showed that band gap energy was reciprocally tuned proportional to the Fe content. The photo-oxidation capability of Fe-doped TiO_2 was found to increase during near-visible light exposure. Use of a macrophage cell line to evaluate cytotoxic and ROS production showed increased oxidant injury and cell death in parallel with a decrease in band gap energy. These findings demonstrate the importance of band gap energy in the phototoxic response of the cell to TiO_2 nanoparticles and reflect the potential of this material to generate adverse effects in humans and the environment during high intensity light exposure.

Keywords

Flame spray pyrolysis (FSP); Nanoparticles; phototoxicity; TiO_2; Fe-doping; band gap energy

Lutz Mädler, Phone: +49 421 218-7737, Fax: +49 421 218-5378, lmaedler@iwt.uni-bremen.de.
[+]These authors contributed equally

Supporting information: The results on the near-visible wavelength used for photoactivation of TiO_2 nanoparticles, X-ray diffraction patterns, FFT images of the Highly resolved TEM, EELS spectrum, illustration of the particle size and crystalline phases, photooxidation of different sizes of pure and 10% Fe doped TiO_2 nanoparticles (adapting new FSP parameters) and extensive explanation of the NATA oxidation is presented. These materials are available free of charge via internet at http://pubs.acs.org

INTRODUCTION

Early identification of material characteristics that could play a role in the potential toxicity of engineered nanomaterials is necessary for safe nanotechnology applications. We recently showed that the mechanistic understanding of ZnO nanoparticle toxicity could be utilized to re-engineer the material to yield particles that are less soluble and less prone to release toxic Zn^{2+}.[1,2] An in depth understanding of mechanisms of potentially hazardous nanomaterial properties is required to develop such safe-by-design strategies. While ZnO nanoparticles were found to be toxic because of dissolution and shedding of toxic Zn^{2+} ions, TiO_2, a relatively dissolution-resistant nanoparticle, has the potential to induce toxicity under UV exposure conditions.[3,4] UV light can excite electrons (e^-) into the conduction band of the TiO_2 nanoparticles leaving behind a hole (h^+) in the valence band. The generated charge could then interact with H_2O and molecular oxygen to generate HO• radical and superoxide, respectively.[3,5–7] However, the intrinsic toxicity of the high energy UV wavelength[5,7] needed to drive this e^-/h^+ pair generation provides a potential obstacle to studying the biological effects of TiO_2 photoactivation.

TiO_2 (crystalline with 80/20 anatase/rutile) with band gap energies of about 3.2 eV requires electromagnetic radiation in the UV range for the generation of e^-/h^+ pair leading to reactive oxygen species (ROS) by photoactivation. Doping with various transition metals that create impurity energy levels within the valence and conduction band of TiO_2 has been shown to facilitate the activation of TiO_2 at low energy wavelength (towards visible light).[8] Several metals (Group IV–VIII) and non-metals (B, C, N, S or I)[9–13] have been used to dope TiO_2 nanoparticles for band gap narrowing and enhancing the photocatalytic activities in the visible range.[14] The band gap narrowing usually requires high dopant level in the semiconductor leading to a different material from the parent oxide.[15] Studies have shown that an appropriate range of Fe-doping in TiO_2 could enhance the photocatalytic property of TiO_2 under light exposure conditions that could partially prevent the recombination of the e^-/h^+ pair[16]. Thus, Fe doping of TiO_2 could provide a possible strategy for elucidating the role of band gap energy in determining the phototoxicity of TiO_2.[17,181619]

In this article, we report the controlled tuning of band gap energies of TiO_2 nanoparticles by incremental loading with Fe during FSP synthesis. These particles were photoactivated at low energy wavelength (350–450 nm) that are not intrinsically toxic to cells. This allowed us to quantitatively demonstrate the generation of harmful free radicals within the cells by photoactivated semiconductor nanoparticles as a paradigm for cell injury.

EXPERIMENTAL SECTION

Synthesis of undoped and Fe-doped TiO_2 nanoparticles

A flame spray pyrolysis technique[20] was used for the production of ultrafine powders of pure and Fe-doped TiO_2 nanoparticles. This was accomplished through the use of the metallorganic precursor titanium (IV) isopropoxide (Strem Chemical, 99.9% pure) with and without Fe napthenate (12% Fe by metal, Strem, 99.9% pure). Titanium (IV) isopropoxide (50 mL) was separately mixed with 0.6–6.5 mL of Fe-napthenate (0.5 M by metal) to make 1–10 at wt % of Fe-doped TiO_2 nanoparticles (for example 6.5 mL of 0.5 M Fe-napthenate was mixed with in 50 mL of 0.5 M titanium (IV) isopropoxide to get 10 at wt % of Fe-doped TiO_2). All the precursors were diluted with xylene (99.95%, Strem) to keep the metal to 0.5 M. For flame spray pyrolysis, the liquid precursor was delivered at the rate of 5 mL/min using a syringe pump and was atomized by a two phase nozzle using 5 L/min O_2 at a constant pressure drop of 1.5 bar at the nozzle tip.[16] The spray was ignited by a premixed co-delivery of CH_4 and O_2 (1.5 L/min, 3.2 L/min) forming a spray flame. The ultrafine particles were formed by reaction, nucleation, surface growth, coagulation and coalescence

in the flame environment. The particles were collected from the 257 mm glass filter placed in the flame reactor at a distance of 60 cm from the flame.

XRD measurements

For the X-ray diffraction measurements, the TiO_2 nanoparticles were loaded into a PANalytical X'Pert MPD PRO diffracting system, equipped with Ni-filtered CuK_α (λ=0.154 nm) radiation, ¼° fixed divergence, primary and secondary Soller slit with 0.04 rad aperture, circular sample holder with 16 mm diameter, and X'Celerator detector, applying a continuous scan in the range of 5–85° 2θ. The structural and microstructural parameters were extracted through Rietveld refinement using the Brass program. [21] Background, scale factor, unit cell parameters, Gaussian as well as Lorentzian half width were simultaneously refined followed by crystalline microstrain analysis. Finally the atomic positions were refined using the structural models ICSD-63710 for rutile and ICSD-63711 for anatase. The determination of the average crystallite sizes (d_{XRD}) was achieved by the line-broadening analysis. The instrumental contribution to the peak broadening was removed by the deconvolution method with crystalline LaB_6 as an instrumental standard.

BET measurements

Nitrogen adsorption-desorption measurements (BET) were carried out at 77K using a NOVA system to determine the specific surface areas. Before the measurements, the samples were degassed at 200°C under vacuum to clean the unwanted adsorbants from the surface. The primary particle size was derived using the equation $d_{\mathrm{BET}}=6/(\rho_p \cdot S_A)$, where d_{BET}, ρ_p and S_A are defined as the average diameter of a spherical particle, theoretical density and the measured specific surface area.

Microscopic imaging

For transmission electron microscopic (TEM) imaging of these particles, samples were first dispersed in absolute ethanol followed by ultrasonification for 1 hour. A drop from the resulting dispersed solution was applied on a TEM grid, evaporated and viewed under the microscope. High resolution transmission electron microscopy images (HRTEM) were obtained with a FEI Titan 80/300 microscope equipped with a Cs corrector for the objective lens, high angle annular dark field detector (HAADF), GATAN post-column imaging filter and a cold field emission gun operated at an accelerating voltage of 300 kV. To obtain an EELS spectrum, the GATAN parallel EELS spectrometer was operated at 0.2 eV per channel as an energy dispersive detector. A Kevex energy dispersive X-ray spectrometer was used at 10 eV per channel for EELS spectra and SAED patterns. Spectra were taken at each sampling point in order to identify the homogeneity of the samples. EFTEM images of pre- and post edges of elemental mappings were obtained from the data by energy calibration and background subtraction. Zero loss spectra were also taken at each sampling point for energy calibration and to identify the homogeneity of the samples.

Band gap energy measurement

UV visible spectroscopy measurements were carried out to determine the band gap energy of the nanoparticles. Finely dispersed TiO_2 nanoparticles in a $BaSO_4$ matrix were pressed between two quartz plates followed by UV measurements in reflection mode using a SHIMADZU UV-vis 2101 PC spectrophotometer. The UV absorbance spectra were used to evaluate the band gap of TiO_2 and Fe-doped TiO_2 nanoparticles by plotting $[F(R\infty)\times h\nu]^{1/2}$ against $h\nu$, where $h\nu$ is the energy of the incident photon and $F(R\infty)$ is the reflection in Kubelka–Munk function. The linear part of the curve was extrapolated to zero reflectance and the band gap energy was derived.

Photo-oxidation measurement and detection of ROS generation

The photo-oxidation capability of TiO_2 nanoparticles was evaluated fluorimetrically using the model substrate *N*-acetyl-L-tryptophanamide (NATA). [22, 23] The nanoparticles (pure and Fe-doped) were initially dispersed in deionised water to prepare a stock solution of 5 mg/mL. A working solution was obtained by diluting 40 μL of the stock solutions with 1 mL of water and sonicating for 15 sec, using a probe sonicator (VibraCell™, Sonics, CT, USA) at 30 mW. The final reaction mixture containing 100 ppm of nanoparticles were mixed with 10 μM NATA. 100 μL of the suspension was transferred to 96 well plates. The plates were illuminated using a xenon arc lamp (Asahi Spectra, Japan) with a light filter that transmits light in the wavelength range of λ = 350–450 nm (Figure S1). Since this wavelength range include the low energy UV plus visible light spectrum, the term "near-visible" [24] is used in this communication and refers to λ = 350–450 nm. The experiment is designed particularly to monitor how samples with various doping concentrations react to a constant amount of incoming light, and to determine how changes in bandgap energy (and therefore changes in total energy available in terms of usable photons) affect cell mechanisms and cell viability.

The rate of decrease in the N-acetyl tryptophanamide (NATA) concentration was monitored by measuring the time dependent loss of fluorescence intensity (excitation/emission 290 nm/350 nm) of the tryptophanyl moiety. For measuring the hydroxyl radical ($HO^{\bullet}$) generation, 100 μg/mL of the nanoparticle suspension were prepared with 10 μM of hydroxyphenyl fluorescein (HPF). The rate of oxidation of HPF was monitored by measuring the intensity of fluorescence emission (excitation/emission 490/515 nm). These experiments were repeated three times with three replicates for each group.

Electron Paramagnetic Resonance (EPR) measurements of hydroxyl radical ($HO^{\bullet}$) generation

Nanoparticles of pure and 10% Fe-doped TiO_2 suspensions in deionized water (100 μg/mL) were mixed with 5-diethoxyphosphoryl-5-methyl-1-pyrroline *N*-oxide (DEPMPO, a spin trap agent for EPR) at a final concentration of 1 μM. 1.5 mL of this freshly prepared mixture was added to a quartz EPR tube (Wilmad Lab-glass, NJ, USA) and illuminated for 10 mins before recording the EPR spectra. The EPR spectrum of the spin adduct of the $HO^{\bullet}$ radical generated by Fenton reaction was used to compare the spectral features of TiO_2 activation. A standard Fenton reaction system (2 mM $FeSO_4$ added to a solution containing 0.1 M PBS, 2 mM DTPA, 2 mM H_2O_2, and 0.1 M DEPMPO) was used as a positive control. EPR measurements were performed in Bruker EMX spectrometer operating at X-band (9.79 GHz with a 100-kHz modulation frequency, 10 mW power, IG modulation amplitude, 8×10^5 receiver gain, 81.92 ms time constant, and 50 G/min sweep rate).

Preparation of nanoparticles in cell culture media

Thawed RAW 264.7 cells (ATCC# TIB71) were cultured in DMEM containing 10% FBS, 100 μg/mL penicillin, 100 μg/mL streptomycin, and 2 mM L-glutamine (Complete DMEM medium). [1] Nanoparticle suspensions (100 μg/mL) were prepared in CDMEM medium for cellular exposure. This was accomplished by adding 20 μL of nanoparticle stock solution (5 mg/mL) in deionized water to 1 mL of CDMEM medium and sonicating for 15 sec at 30 mW. Particle size distribution (PSD) and zeta potential of the nanoparticles in water and CDMEM were assessed using a ZetaSizer Nano (Malvern Instruments, Westborough, MA, USA) in the backscattering mode.

Transmission electron microscopy (TEM) to assess the cellular uptake of nanoparticles

RAW 264.7 cells treated with pure and 10% Fe-doped TiO_2 were subjected to TEM to examine if there was any distinct difference in the uptake pattern of these nanoparticles.

RAW 264.7 cells grown in 6 well plate overnight received 100 μg/mL of TiO_2 or the particles doped with 10% Fe. After incubation for 24 hrs in standard cell culture conditions, the cells were washed three times using phosphate buffered saline (PBS) to remove loosely associated nanoparticles from cell surface. These cells were fixed with 2.5% glutaraldehyde in PBS and washed. After postfixation in 1% OsO_4 in PBS for 1 hr, the cells were dehydrated in a graded series of ethanol, treated with propylene oxide and embedded in Epon. The sections in the range of 60–70 nm thick sections were cut on a Reichert-Jung Ultracut E ultramicrotome and transferred to Formvar-coated copper grids. These sections were stained with uranyl acetate and Reynolds lead citrate and examined on a JEOL 100CX electron microscope at 80 kV in UCLA BRI Electron Microscopy Core facility.

Measurement of cellular response to light illumination after nanoparticle treatment

RAW 264.7 cells were plated at 5,000 cells per well in 384 well plates (CellBound, Corning Inc, MA, USA) and grown to 80% confluency overnight at 37°C in a 5% CO_2 incubator. 50 μL of the nanoparticle suspension at the concentration of 100 μg/mL was added to each well of the 384 well plates. The nanoparticle added cells were incubated for 24 hrs in standard cell culture conditions. After the incubation period, the cells were washed three times with PBS. After the final wash, the wells received 25 μL of PBS and six wells from each group were exposed to near-visible light for 20 min. In another set of experiments, cells being treated with nanoparticles received 100 μM of N-acetyl cysteine (NAC) and were illuminated as previously. Following illumination for 20 mins, PBS was replaced with CDMEM and the cells were incubated for another three hours.

These cells were assayed for toxic oxidative stress by contemporaneously recording mitochondrial superoxide generation, lowering of mitochondrial membrane potential and loss of viability using a high content screening assay. Cells in the 384 well plate subjected to nanoparticle and/or light treatment were added with 25 uL of dye cocktails containing MitoSox Red, JC1 and propidium iodide in combination with Hoechst 33342 for assaying mitochondrial superoxide generation, loss of mitochondrial membrane potential and loss of cell viability, respectively. [2] Fluorescence images of the cells were acquired using an epifluorescence microscope- Image-Xpress^{micro} (Molecular Devices, Sunnyvale, CA). Images from the microscope were analyzed using MetaXpress software (Molecular Devices, Sunnyvale, CA) to score % cells positive for each cytotoxicity parameter. Hoechst 33342, which stains all the nuclei, was used to count the total number of cells using the following setting in the blue channel: approximate minimum width was 3 μm (about 3 pixels); the approximate maximum width was 10 μm (about 7 pixels); the threshold intensity above background level was 100 gray levels. In the green (JC-1) and red (PI and MitoSox Red) channels the minimum width was set at 5 μm (about 6 pixels) and the approximate maximum width was 30 μm (about 22 pixels). The threshold intensities above background were set at 250 and 500 gray levels respectively for the green and red channels. The cells regarded as positive were calculated as the % of cells with an above threshold response compared to the total number of Hoechst 33342 positive cells. The experiments were repeated thrice with six replicates in each group. The statistical significance was calculated using paired t-test.

RESULTS

Synthesis, Physicochemical characterization and UV visible spectroscopy

Pure and Fe-doped TiO_2 nanoparticles were prepared using versatile flame spray pyrolysis (FSP) technique. In order to obtain reduced band gap energy, the Fe must be homogenously distributed within a crystalline TiO_2 matrix. TEM images (Figure 1a) confirm the indistinguishable crystalline morphology of the pure and Fe-doped TiO_2 particles in the

range of 9–20 nm. The highly crystalline nature of these particles was evident from the distinct SAED crystallographic rings (Figure 1a, right column), HRTEM images (lattice fringes of 0.355, 0.353 and 0.324 nm spacing with respect to anatase, 4 at wt% Fe-doped TiO_2 (4% of Fe in Ti by metal) and rutile) and X-ray diffraction patterns (Figure S2). The fourier filtered HRTEM images (Figure S3) reveal highly resolved power spectra with clear crystallographic arrangements of the particles. [4, 25, 26] In order to verify the homogenous distribution of Fe in TiO_2 matrix, energy filtered transmission electron microscopy (EFTEM) (Figure 1b) and electron energy loss spectra (EELS) (Figure S4) in STEM mode were conducted. These analyses clearly demonstrate the homogeneous distribution of the Fe in the parent matrix. The Ti L-edge arises from the *d*-*d* transitions of *d* electrons into the unoccupied 3*d*-states. Two well-separated strong lines at energy loss positions of 462.5 and 467.5 eV and one weak shoulder at 465.9 eV corresponds to the characteristic Ti-L edge of Ti in the homogeneous sample (Figure S4). Comparing the spectral features of the absorption edge from the Fe-doped TiO_2 nanoparticles, the two peaks in the energy range between 712 and 724 eV can be assigned to the Fe^{2+} or Fe^{3+} ions. [27–29]

At constant FSP reactor conditions (5 mL/min precursor flow, 5L/min O_2), Fe doping of TiO_2 has additional effects besides the anticipated band gap engineering: (1) the equivalent primary particle size (d_{BET}) and the crystallite size (d_{XRD}) decrease and (2) the anatase to rutile ratio decreases with an increase in Fe loading (0–10%) (Figure S5a) (a typical observation for a FSP synthesized TiO_2 nanoparticles). Thus, the average particle size derived from BET (d_{BET}) and XRD (d_{XRD}) ranged from 11 to 5 nm and from 12 to 6 nm respectively, for different Fe loadings. In order to equalize the size of doped and undoped nanoparticles, additional nanoparticle samples were prepared at modified reactor conditions (5 mL/min precursor flow, 6L/min O_2 for pure TiO_2 and 5 mL/min precursor flow, 4L/min O_2 for 10 at wt% Fe-doped TiO_2). This resulted in doped and undoped TiO_2 nanoparticles with d_{BET} = 7 nm for TiO_2 and 12 nm for 10 at wt% Fe-doped TiO_2 (Figure S5b) enabling investigations of possible particle size effects on photocatalytic property of pure and doped TiO_2.

UV-visible spectra were recorded for pure and Fe-doped TiO_2 nanoparticles in order to demonstrate the lowering of the band gap energy after Fe doping. Figure 2a shows the modified Kubelka–Munk reflection plots derived from the UV visible spectra in the reflection mode. The bandgap energy (E_g) values for undoped and Fe-doped TiO_2 nanoparticles range from 3.3 to 2.8 eV. Increasing the Fe content in TiO_2 shifts the band gap energy towards longer wavelengths (Figure 2b) due to the creation of trap levels between the conduction and valence bands of TiO_2. [30, 31]

Photocatalytic property of band gap tuned TiO_2

The generation of e^-/h^+ pairs in band gap tuned TiO_2 during near-visible light illumination (lower energy spectrum, see Figure S1 for exact wave length range) was investigated by means of the reduction in the NATA fluorescence intensity. During photoactivation of TiO_2 in presence of NATA, the oxidation is mediated by its direct interaction with the nanoparticle surface and/or by the reactive oxygen species generated during the process. Figure 3(a) shows an increase in the rate of NATA oxidation during illumination of Fe-doped TiO_2. This is indicative of a photochemical reaction by near-visible light in the doped particles. The increase in NATA oxidation was abrupt at 1 % of Fe doping and stabilized at a doping level of 6 %. Notably, the NATA oxidation was accompanied by decrease in $HO^{\bullet}$ radical production with incremental levels of Fe (Figure 3b). Hydroxyphenyl fluorescein (HPF) oxidation studies as well as EPR measurements (Figure 4) also confirmed decreased $HO^{\bullet}$ radical generation during illumination of Fe-doped TiO_2. This combination of increased NATA oxidation with decreased $HO^{\bullet}$ radical generation during illumination of Fe-doped

TiO_2 suggest different reactivity mechanisms of the e^-/h^+ pairs formed in pure and Fe-doped TiO_2 (detailed in discussion).

It is noteworthy that the primary particle size of TiO_2 decrease gradually with doping concentrations as previously called out in Figure S5b. Therefore, to investigate a possible size effect in the photo-oxidation activity of the nanoparticles, it was necessary to study pure and 10% Fe-doped TiO_2 at different size ranges. This demonstrated that an increase in particle size increases the photocatalytic property of both doped and undoped TiO_2 (Figure S6). From the result, it is evident that the increased photo-oxidation capacity of doped TiO_2 is not primarily due to the primary particle size reduction but due to tuning of the band gap energy.

Nanoparticle suspensions in water and CDMEM (cell culture medium) prepared as detailed in the materials and method section were assayed for agglomeration size using DLS. Data showed that the decrease of agglomerate size with the increasing Fe content (see Figure S7). Interestingly, the zeta potential measurement showed an increase in the negative surface charge in Fe doped TiO_2. Therefore, we envisage that the net reduction in the agglomeration size of Fe doped TiO_2 is caused by the electrostatic repulsive force. (Figure S7)

The biologic phototoxic effect of Fe-doped TiO_2 nanoparticles

For this phase of the study a macrophage cell line for exposure to TiO_2 nanoparticles was used. Initially, the effects of cells exposed to nanoparticles or to light treatment alone (LC) were compared. This demonstrated that exposure to nanoparticles or near-visible light illumination alone had no significant effect on cell viability as determined by cell viability (PI uptake) assay (Figure 5a). By contrast, cellular exposure to UV light in the range (280–350) was toxic, thereby confirming the necessity to use Fe-doping to study the cytotoxic potential of light-activated TiO_2 (data not shown). However, combining the effects of nanoparticle with near visible light exposure clearly demonstrated increased PI uptake in RAW 264.7 cells (Figure 5a). Moreover, the data demonstrated that this cytotoxic effect was incremental with increased levels of Fe-doping as well as in increasing the light dose (240–1600 mJ/cm^2). Thus, while three minutes of illumination was insufficient in inducing increased cell death, the % of dead cells increased significantly with 10–20 mins of illumination. In contrast, pure TiO_2 failed to respond to increasing light dose. In order to demonstrate that this difference was not due to differences in cellular uptake, we also performed transmission electron microscopy (TEM) of cells treated with pure and 10% Fe-doped nanoparticles (Figure 5b). As shown in the left panels there was no obvious difference in the uptake of doped and undoped TiO_2 nanoparticles. Notably, both types of nanoparticles were taken up into phagosomes, as demonstrated in the panels on the right hand side (Figure 5b). Interestingly, the agglomerate sizes of particles associated with cells (both outside and inside the cells) showed comparable size range (see TEM images, Fig S8). Inside the cells, majority of the nanoparticle agglomerates were physically associated with the phagosome membranes (red arrow- right column). However, it should be noted that cellular uptake of nanoparticle may not be absolute requirement to cause cytotoxicity. Nanoparticles outside the cells but associated with cell membrane or those in near vicinity to cells (as seen in TEM of Fig S8) could also contribute to cell toxicity upon photoactivation. This is because the generated ROS could either act directly on cell membrane components to impair the membrane integrity or some of the ROS such as H_2O_2 can trespass the membrane boundary to induce oxidative stress and subsequent cellular injury.

Because photo-oxidation and e^-/h^+ pair generation is accompanied by ROS generation, we also looked into more depth as to whether the increased PI uptake is accompanied by mitochondrial superoxide generation and loss of mitochondrial membrane potential as incorporated by our recently developed multi-parametric high throughput screening (HTS)

assay. [2] Figure 6a shows an increase in each of the multi-parameter responses (increase in the population of cells with depolarized mitochondria, and decreased mitochondrial membrane potential (DMMP)) with incremental levels of Fe doping and use of 10 mins of near-visible illumination. In order to verify the role of oxidative stress in this multi-parametric response, the experiments were repeated in presence of N-acetyl cysteine (NAC)- a known free radical quencher and glutathione precursor. Figure 6b shows that cells pre-treated with NAC failed to elicit any ROS generation, mitochondrial depolarization and decreased mitochondrial membrane potential (DMMP). This confirms that oxidative stress indeed plays a role in the TiO_2 photo-oxidation effect on cells.

DISCUSSION

Successful incorporation of an Fe-dopant in the crystal lattice of the parent TiO_2 nanoparticles plays an important role in controlling their photoactivity. In the present investigation, Fe^{3+} was substitutionally doped in the TiO_2 matrix. The homogeneous distribution as seen from EFTEM (Figure 1) and EELS assessment of the Fe^{3+}-edge (Figure S4) confirms the presence of vacant 3*d*- orbitals for trapping electrons during excitation. Transition metals such as Fe lower the band gap energy by introducing trap levels between the valence and conduction bands of TiO_2. These trap levels allow for excitation of electrons when subjected to near-visible light illumination (Figure 2). The lower absorption edge of Fe^{3+}-doped TiO_2 seen in the present investigation is due to the charge-transfer transition between the Fe^{3+}-*d* electrons and the conduction or valence band of TiO_2.[32] The electronic transitions from the valence band to dopant level or from the dopant level to the conduction band can effectively red shift the band edge adsorption threshold. [30] The higher energy state of 3*d*-electrons from Fe-dopant (relative to the ground state electrons of TiO_2) could be easily excited to the conduction band of TiO_2 nanoparticles.

Figure 7 depicts the general reaction mechanism of the Fe-doped TiO_2 nanoparticles exposed to the abiotic or biotic systems during light illumination. During light illumination of the doped or undoped nanoparticles, the electrons are transferred to the conduction band or to the vacant 3*d* orbital of Fe^{3+} (trap levels) as evidenced from EFTEM and EELS measurements. The production of hydroxyl radical responsible for the oxidation of biomolecule takes place by two mechanisms (1) electron (2) hole driven hydroxyl radical. Considering the mechanism related with electrons to the doped particles, the electrons in the trap level reduces Fe^{3+} to unstable Fe^{2+} which releases electrons in the process to gain ionic stability (oxidation). These electrons are transferred to the surface molecular dioxygen to generate superoxide radicals. This reactive oxygen species attack molecules from the environment (e.g. water) and can produce oxidizing agents (e.g. H_2O_2) followed by hydroxyl radical generation in the presence of light. In the case of biotic systems exposed to the nanoparticles, H_2O_2 immediately oxidizes biomolecules releasing an electron. In abiotic conditions, the H_2O_2 reacts with Fe^{4+} (oxidation by gaining an electron) producing stable Fe^{3+} in the trap levels within the nanoparticle. In the second case, the holes reacts with the water molecules adsorbed on the surface of the nanoparticles producing H^+ ions and $HO^{\bullet}$. Hydrogen ions are stabilized by the electrons released from the oxidation of Fe^{2+} to Fe^{3+} and hydroxyl radical is responsible for the oxidation of the biomolecules. This principle of photoxidation is demonstrated in detail below considering a biomolecule (NATA) oxidation during near-visible light illumination.

In addition to the chemical composition, the physical arrangement of the atoms and the particles size may influence the photochemical behavior. The difference in orientation of crystal planes in doped and undoped TiO_2 particles may lead to differences in surface atomic arrangements and coordination resulting in differential photocatalytic activity.[33, 34] Our XRD data suggest the increase in rutile phase as Fe was increased from 0–10 at wt%

[see Figure S2]. Anatase TiO_2 has larger band gap energy than rutile, which is considered to be more photoactive due to higher electron mobility.[35] It is noteworthy that the sizes of Fe doped nanoparticles decreased gradually along the doping concentration [Figure S5 (a)]. Even if we consider the recently demonstrated heterostructure of pure anatase/rutile crystals, [36] the increased activity will not be observed in the wavelength range used in our present study. This tendency was also reflected in the agglomeration size of nanoparticles suspended in water and CDMEM medium [Figure S7 (a) and (b)]. Earlier studies by Wang *et al.* indicates the possibility of charge/electron transfer across adjacent particles in nanoparticle agglomerate.[37] This 'relay effect' could facilitate the oxidation of substrate (*e.g.* NATA or biomolecules) remote from the original particle absorbing the light energy. Particle size is generally an important parameter for photocatalysis since it directly impacts the specific surface area. Decrease in particle size could lead to increased specific surface area and potentially expose more surface reactive sites. However, the possibility of higher electron-hole pair recombination in small sized nanoparticles could override the increase in surface reactive sites and may lead to decreased photocatalytic action in smaller particles. Consistently, the photooxidation of NATA was higher for the larger size particles of pure and Fe doped TiO_2. In short, the photocatalytic efficiency does not monotonically increase with decreasing particle size [18] and can also not be ascribed to the differences in physical properties of TiO_2 and Fe doped TiO_2 that contribute to the observed NATA oxidation by Fe doped TiO_2; instead, the photocatalytic activity is due to decrease in band gap energy.

During photo-oxidation of NATA (a model biomolecule used in Figure 3) in presence of doped TiO_2 nanoparticles, a gradual increase in the photo-oxidation with a decrease in band gap energy was observed. In pure TiO_2, the generation of ROS species is probably mediated by the electron transfer between the excited TiO_2 and adsorbed molecular oxygen, which ultimately leads to oxidation of NATA. [38] In the case of doped nanoparticles (Figure S9), the electron excited to the conduction band is taken up by Fe^{3+} and reduces superoxide generation as well as the recombination of e^-/h^+ pair. Figure S9 depicts NATA oxidation and is therefore a specific example of the events. Holes (h^+) in the valence band abstract an electron from surface associated NATA, leading to NATA oxidation. Alternately, the simultaneous redox process of trapping electrons in the Fe^{3+} states is enhanced by surface molecular dioxygen to produce ROS.[39] These species react with charged NATA molecules to form phenyl oxidized NATA. [40] The subsequent oxidized and unstable Fe^{4+} species are immediately reduced to Fe^{3+} by electron transfer from the excited NATA molecule during light illumination. The production of the hydroxyl radical is also enhanced by the reaction of holes with the water adsorbed on the particle surface. The electron transfer from the oxidation of ferric ion to ferrous ion neutralizes the hydrogen ion during the reaction. The increase in photo-oxidation and decrease in ROS generation for Fe-doped TiO_2 under near-visible light indicates the significant interaction of the impurity levels (Fe-traps) for NATA oxidation (Figure 3). The analysis of the EPR hyperfine splitting constants for spin adducts of DEPMPO showed signature prints of $HO^{\bullet}$ radicals being produced, corroborating the proposed mechanism (Figure 4). As indicated by the peak intensity, $HO^{\bullet}$ radical generation was reduced by Fe-doping. Furthermore, the decrease in $HO^{\bullet}$ radical generation with increasing Fe loading during NATA oxidation also supports this mechanism (Figure 3(b)). During direct oxidation of NATA, the trapped Fe^{3+} donates electrons to the surface oxygen to generate more ROS for the photochemical reaction (Figure S9). Thus, the decreasing ROS generation along with the increasing Fe content suggests the photo-oxidation in Fe-doped TiO_2. The process of oxidation is a combined effect of particle surface catalytic phenomena aided by Fe^{3+} and ROS. Here, it was clearly demonstrated that Fe-doped TiO_2 can be excited under UV to visible light and the photo-oxidation capability of doped TiO_2 is improved by lowering the band gap energy. This provides the knowledge base for interpreting the cellular responses to Fe-doped TiO_2 under light illumination.

Fe doping allowed the photo-toxic effect of TiO_2 to be studied under non-toxic light exposure conditions. A model mammalian cell line (RAW 264.7) was used to elucidate the role of bad gap energy in the photo-toxic response to doped TiO_2. Initially the toxicity induced due to pure and band gap tuned TiO_2 was measured with increasing light exposure time (e.g. dose). First, it was confirmed that the cells show no effect when subjected to the particles without light (data not shown). Second, it was confirmed that the cells show no effect due to incremental illumination doses in the absence of particles (Figure 5a). Third, it was confirmed that the photon energy (85% below 3.2 eV) was substantially lower than the band gap of pure TiO_2 and therefore pure TiO_2 failed to show cytotoxicity in RAW 264.7 cells under near-visible light illumination condition (Figure 5a). This further confirms our hypothesis of required electron transfer into the conduction band for photochemical activation. In contrast to pure TiO_2, Fe-doped particles showed a light dose-dependent increase in cytotoxicity. The absence of cell death at three minutes of light illumination suggest the requirement of a critical dose of e^-/h^+ pair and free radical generation to induce cytotoxicity. The magnitude of cell death was correlated with the reduction in band gap energy of TiO_2. This demonstrates that, the decrease in the band gap by higher dopant levels allows a more efficient utilization of the light energy for biological response generation. Correlating Figure S1 and Figure 2 it is evident that only the nanoparticles with two highest loadings of iron can fully utilize the light energy for e^-/h^+ pair generation. In addition, the magnitude of cell death also increased when higher light dose was utilized suggesting a direct influence on the photocatalytic property of Fe-doped TiO_2 (light dose dependant). In order to exclude other mechanisms besides photoactivation, uptake and bioavailability of these nanoparticles were also investigated. Microscopic analyses showed that agglomerates of nanoparticles are taken up into cells through phagocytosis irrespective of their Fe content (Figure 5(b)). These observations agree with Singh *et al*. who described the association of agglomerated TiO_2 with cell membranes and their uptake through phagocytosis. [41, 42] Although Geiser *et al*. reported the possibility of direct interaction of TiO_2 nanoparticles with subcellular organelles such as the nucleus [43] we obtained no indication of the direct association of nanoparticles with any vital organelles. However, both types of nanoparticles were observed to be closely associated with the lipid bilayer boundary of the phagosome. Thus, the TEM studies showed that the mechanism of uptake and bioavailability is not markedly different in pure and band gap tuned TiO_2 nanoparticles and the difference in toxicity is unlikely due to differences in the uptake mechanism.

In order to understand the influence of e^-/h^+ pair in the molecular mechanism of cytotoxicity, [44] we studied cellular oxidative stress responses. Intracellular ROS generation and oxidative stress is recognized as a major injury paradigm in response to exposure to redox-active nanomaterials. Therefore the inter-linked cytotoxic oxidative stress response as determined by studying mitochondrial superoxide generation, mitochondrial depolarization, and cell membrane leakage was measured. The redox-active nature of band gap tuned TiO_2 was demonstrated by NATA oxidation studies (Figure 3, 4 and S9). The % of responding cells in each category was contemporaneously increased by Fe-doping (Figure 6a). The definite role of oxidative stress in the induction of cell death was evident by the effect of NAC pretreatment which almost totally reversed the cytotoxic effects (Figure 6b). The lowering of band gap energy by Fe doping allows excitation of valence electrons to vaccant *d*-orbitals in Fe^{3+}, reducing it to unstable Fe^{2+} followed by electron release to biomolecules (Figure 7). Since the TiO_2 agglomerates inside the cell are in direct contact with the phagosome membrane, it is possible to oxidize membrane associated proteins as well as induce lipid peroxidation free radicals. When the magnitude of free radical generation is sufficient enough to overcome cellular antioxidant defense, damage to a host of biomolecules could trigger additional cellular responses such as mitochondrial perturbation and cytotoxicity.[2, 45] The increase in inter-linked cytotoxic events with decreasing band gap energy of TiO_2 thus provides evidence of wave length dependant phototoxicity of doped

TiO_2. In addition to the induction of oxidative stress due to photo-oxidation of biomolecules in the cells, there is a possibility of $OH^{\bullet}$ generation via the Fenton reaction as a result of Fe^{2+} shedding from the doped TiO_2 particles in the acidifying endosomal compartments. However, in the absence of light illumination of Fe-doped TiO_2, no significant contribution of Fenton reactions to cytotoxicity was observed. Thus by combining results from the physicochemical characterization, photo-oxidation of NATA and oxidative stress dependent cell death, our studies clearly demonstrate that the band gap dependent free radical generation is playing an important role in the phototoxic potential of TiO_2.

CONCLUSION

We demonstrated a material synthesis and design strategy to enable us to study the potential harmful effects of TiO_2 photooxidation in tissue culture cells. The specific design of Fe-doped TiO_2 nanoparticles using versatile and a reproducible flame spray pyrolysis (FSP) technique enabled us to introduce trap levels and band gap tuning to study photoactivation under near-visible wavelength conditions. Reaction pathways involving pure and Fe-doped TiO_2 nanoparticles during near-visible illumination demonstrated the role of $e^{+}h^{-}$ pair in the induction of phototoxicity. Oxidative stress induced cell death increased gradually with the decrease in band gap energy that allowed progressively more ROS generation and biological oxidant injury under less toxic near-visible illumination conditions. The biological oxidative stress response is a tiered event that could be recorded by a series of sublethal and lethal assays in a multi-parametric screening process. The progressive increase in lethal and sublethal response generation is a reflection of the increased oxidant potential of TiO_2 due to a decrease in band gap energy under these illumination conditions. The significant reduction of oxidative stress in the presence of a thiol precursor and radical scavenger (NAC) further serves to illustrate the importance of oxidant injury during TiO_2 photo-oxidation. Because of the proven ability of the FSP to obtain nanoparticles less than 10 nm and by that the photoactivation performance under tissue culture conditions, the proposed method could be a general technique to investigate the phototoxicity evaluation in real-life exposure environments such as TiO_2 uptake in plants or environmental life forms exposed to bright sunlight.

Supplementary Material

Refer to Web version on PubMed Central for supplementary material.

Acknowledgments

This material is based upon work supported by the National Science Foundation and the Environmental Protection Agency under Cooperative Agreement Number DBI-0830117. Any opinions, findings, and conclusions or recommendations expressed in this material are those of the author(s) and do not necessarily reflect the views of the National Science Foundation or the Environmental Protection Agency. This work has not been subjected to EPA review and no official endorsement should be inferred. Key support was provided by the US Public Health Service Grants U19 ES019528 (UCLA Center for NanoBiology and Predictive Toxicology), RO1 ES016746, and RC2 ES018766. Authors SP and LM would like to thank the group of Prof. A. Rosenauer and M. Schowalter, Department of Physics, and University of Bremen for Microscopy, EFTEM and EELS measurements and Prof. M. Bäumer for UV-Visible spectroscopic measurements

References

1. Xia T, Kovochich M, Liong M, Mädler L, Gilbert B, Shi H, Yeh JI, Zink JI, Nel AE. ACS Nano. 2008; 2:2121–2134. [PubMed: 19206459]
2. George S, Pokhrel S, Xia T, Gilbert B, Ji ZX, Schowalter M, Rosenauer A, Damoiseaux R, Bradley KA, Mädler L, Nel AE. ACS Nano. 2010; 4:15–29. [PubMed: 20043640]
3. Hoffmann MR, Martin ST, Choi W, Bahnemann DW. Chem Rev. 1995; 95:69–96.

4. Lu N, Zhu Z, Zhao X, Tao R, Yang X, Gao Z. Biochemical and Biophys Res Commun. 2008; 370:675–680.
5. Kramer GF, Ames BN. J Bacteriol. 1987; 169:2259–2266. [PubMed: 3553161]
6. Long TC, Saleh N, Tilton RD, Lowry GV, Veronesi B. Environ Sci & Technol. 2006; 40:4346–4352. [PubMed: 16903269]
7. Sinha RP, Hader DP. UV-induced DNA damage and repair: a review. Photochem & Photobiol Sci. 2002; 4:225–236. [PubMed: 12661961]
8. Zhu Y, Zhang L, Yao W, Cao L. Appl Surface Sci. 2000; 158:32–37.
9. Asahi R, Morikawa T, Ohwaki T, Aoki K, Taga Y. Science. 2001; 293:269–271. [PubMed: 11452117]
10. Choi W, Termin A, Hoffmann MR. J Phys Chem. 1994; 98:13669–13679.
11. Cong Y, Zhang J, Chen F, Anpo M, He D. J Phys Chem C. 2007; 111:10618–10623.
12. Hong X, Wang Z, Cai W, Lu F, Zhang J, Yang Y, Ma N, Liu Y. Chem Mater. 2005; 17:1548–1552.
13. Zhao W, Ma W, Chen C, Zhao J, Shuai Z. J Am Chem Soc. 2004; 126:4782–4783. [PubMed: 15080674]
14. Thompson TL, Yates JT. Chem Rev. 2006; 106:4428–4453. [PubMed: 17031993]
15. Serpone N. J Phys Chem B. 2006; 110:24287–24293. [PubMed: 17134177]
16. Teoh WY, Amal R, Mädler L, Pratsinis SE. Catal Today. 2007; 120:203–213.
17. Wang, C-y; Bahnemann, DW.; Dohrmann, JK. Chem Commun. 2000; 16:1539–1540.
18. Zhang Z, Wang C-C, Zakaria R, Ying JY. J Phys Chem B. 1998; 102:10871–10878.
19. Teoh WY, Mädler L, Beydoun D, Pratsinis SE, Amal R. Chem Eng Sci. 2005; 60:5852–5861.
20. Teoh WY, Amal R, Madler L. Nanoscale. 2010; 2:1324–1347. [PubMed: 20820719]
21. Birkenstock, J.; Fischer, RX.; Messner, T. BRASS. The Bremen Rietveld Analysis and Structure Suit. 2009. http://www.brass.uni-bremen.de/
22. George S, Kishen A. J Bio Optics. 2007; 12:10.
23. Lambert CR, Reddi E, Spikes JD, Rodgers MAJ, Jori G. Photochem Photobiol. 1986; 44:595–601. [PubMed: 3809256]
24. Kubitschek HE. Science. 1967; 155:1545–1546. [PubMed: 5335927]
25. Daoud WA, Xin JH, Pang GKH. J Am Ceram Soc. 2005; 88:443–446.
26. Reyes-Coronado D, Rodriguez-Gattorno G, Espinosa-Pesqueira ME, Cab C, de Coss R, Oskam G. Nanotechnology. 2008; 19:10.
27. Bordat C, Sich M, Rety F, Bouet O, Cournot G, Cuenod CA, Clement O. J Mag Res Imag. 2000; 12:505–509.
28. Kuiper P, Searle BG, Duda LC, Wolf RM, van der Zaag PJ. J Electr Spectros Rel Phenomena. 1997; 86:107–113.
29. Moulin CCD, Rudolf P, Flank AM, Chen CT. J Phys Chem. 1992; 96:6196–6198.
30. Nagaveni K, Hegde MS, Madras G. J Phys Chem B. 2004; 108:20204–20212.
31. Serpone N, Lawless D, Disdier J, Herrmann JM. Langmuir. 1994; 10:643–652.
32. Litter MI, Navío JA. J Photochem Photobio A: Chem. 1996; 98:171–181.
33. Hotsenpiller PAM, Bolt JD, Farneth WE. J Phys Chem B. 1998; 102:3216–3226.
34. Ohno T, Sarukawa K, Matsumura M. New J Chem. 2002; 26:1167–1170.
35. Kera, YKH.; Murakami, S. Photocatalysis: Science and Technology. Kaneko, M.; Okura, I., editors. Kodansha, Springer; Tokyo: 2002. p. 29-49.
36. Kho YK, Iwase A, Teoh WY, Mädler L, Kudo A, Amal R. J Phys Chem C. 2010; 114:2821–2829.
37. Wang, C-y; Böttcher, C.; Bahnemann, WD.; Dohrmann, KJ. J Mater Chem. 2003; 13:2322–2329.
38. Nosaka Y, Daimon T, Nosaka AY, Murakami Y. Phys Chem Chem Phys. 2004; 6:2917–2918.
39. Tachikawa T, Fujitsuka M, Majima T. J Phys Chem C. 2007; 111:5259–5275.
40. Simat TJ, Steinhart H. J Agr Food Chem. 1998; 46:490–498. [PubMed: 10554268]
41. Churg A, Stevens B, Wright JL. Am J of Physiol - Lung Cell and Mol Physiol. 1998; 274:L81–L86.

42. Singh S, Shi T, Duffin R, Albrecht C, van Berlo D, Höhr D, Fubini B, Martra G, Fenoglio I, Borm PJA, Schins RPF. Toxicol Appl Pharmacol. 2007; 222:141–151. [PubMed: 17599375]

43. Geiser M, Rothen-Rutishauser B, Kapp N, Schürch S, Kreyling W, Schulz H, Semmler M, Hof VI, Heyder J, Gehr P. Environ Health Perspect. 2005; 113:1555–1560. [PubMed: 16263511]

44. Linsebigler AL, Lu G, Yates JT. Chem Rev. 1995; 95:735–758.

45. Nel A, Xia T, Madler L, Li N. Science. 2006; 311:622–627. [PubMed: 16456071]

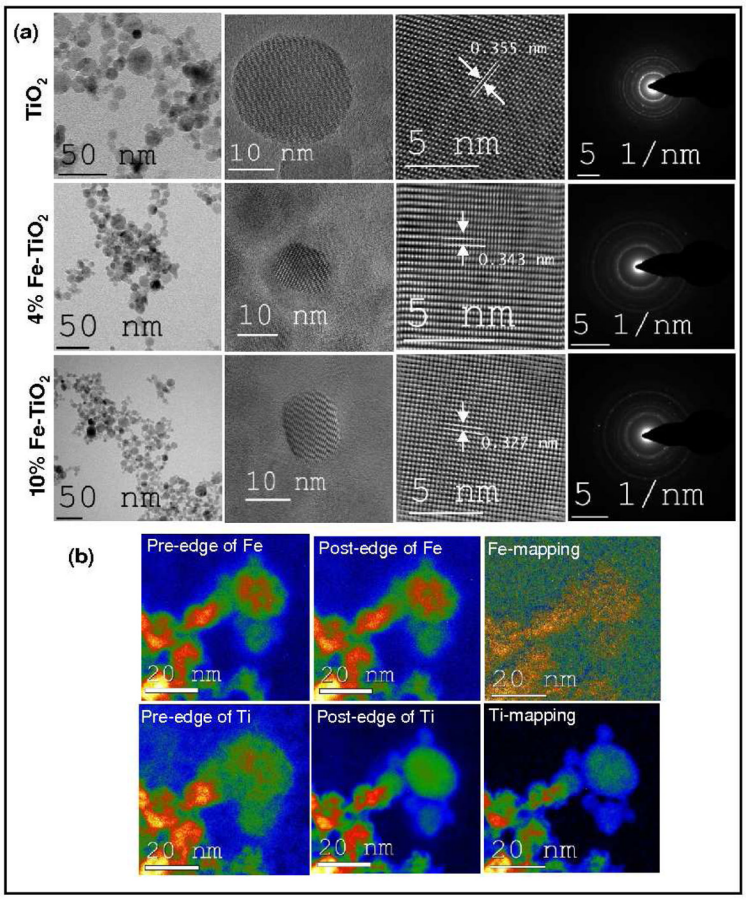

Figure 1.

Microscopic imaging of undoped and Fe doped TiO_2 nanoparticles. (a): Low resolution, high resolution imaging of single particles, magnified portion of the particle and respective SAED patterns of; Undoped TiO_2 (upper panel); 4 at wt % Fe doped TiO_2 (middle panel) and; 10 at wt % Fe doped TiO_2 nanoparticles (Lower panel).

(b) The Energy filtered transmission electron microscopic images of 10 at wt % Fe doped TiO_2 nanoparticles. The pre and post edge along with elemental mapping (Fe and Ti) clearly show that Fe is homogeneously distributed in the TiO_2 matrix.

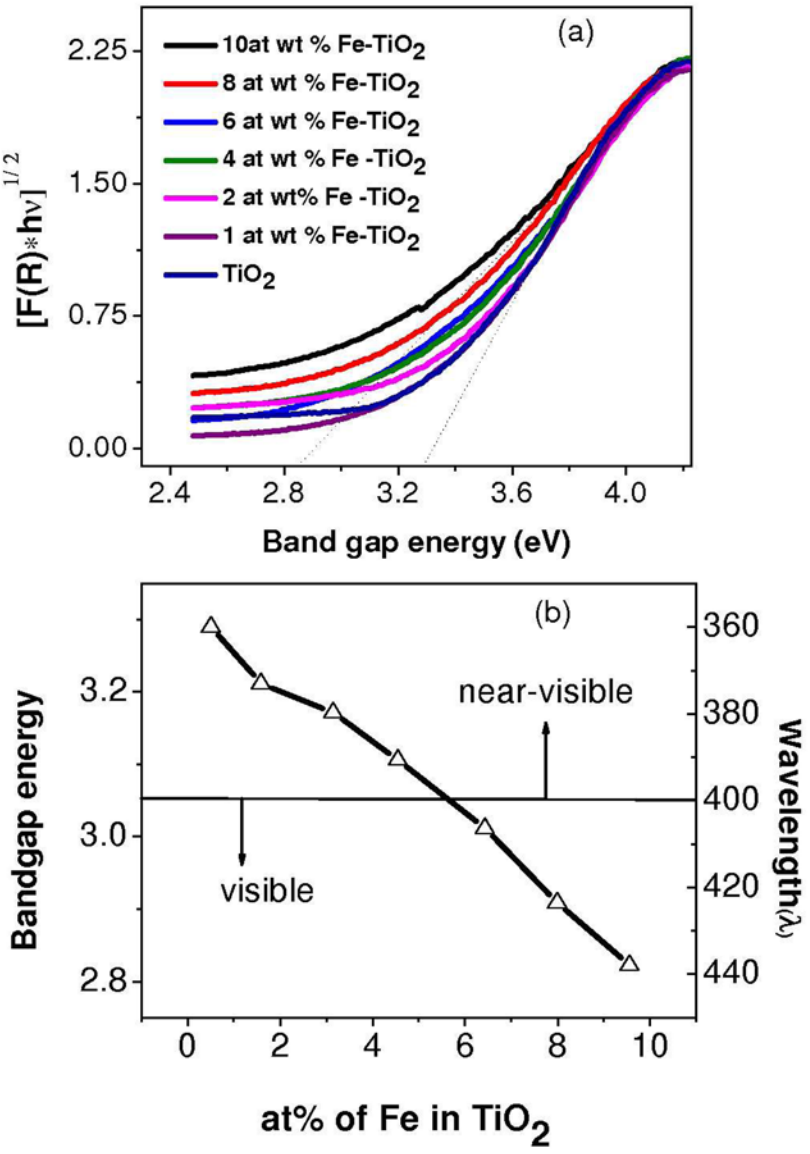

Figure 2.

Photochemical characterization of nanoparticles. (a) UV-visible spectroscopic measurements and subsequent Kubelka–Munk reflection plots for undoped and Fe doped TiO_2 nanoparticles. (b) The band gap energy tuning by Fe doping in the TiO_2 matrix. The band gap energy decreases with increasing concentration of Fe in the TiO_2 lattice.

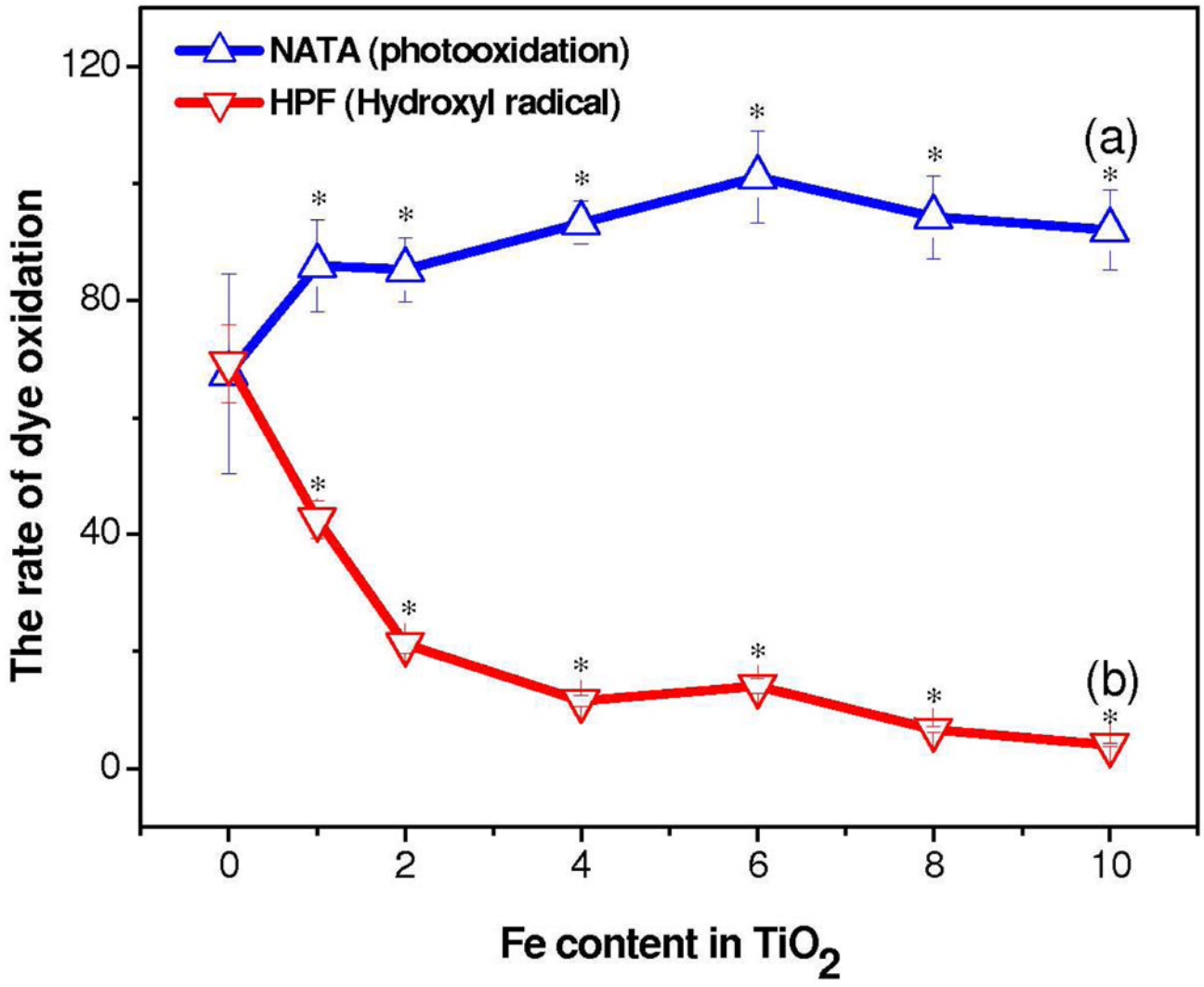

Figure 3.

(a) Photo-oxidation capability (b) hydroxyl radical generation during near-visible light irradiation to the TiO_2 nanoparticles. Nanoparticles (100 ug/mL) were suspended in water in presence of indicator dyes followed by illumination for 10 mins. The rate of photo-oxidation, was measured in terms of N-acetyl-L-tryptophanamide (NATA) oxidation. * statistically significant from 0% Fe $p \leq 0.05$.

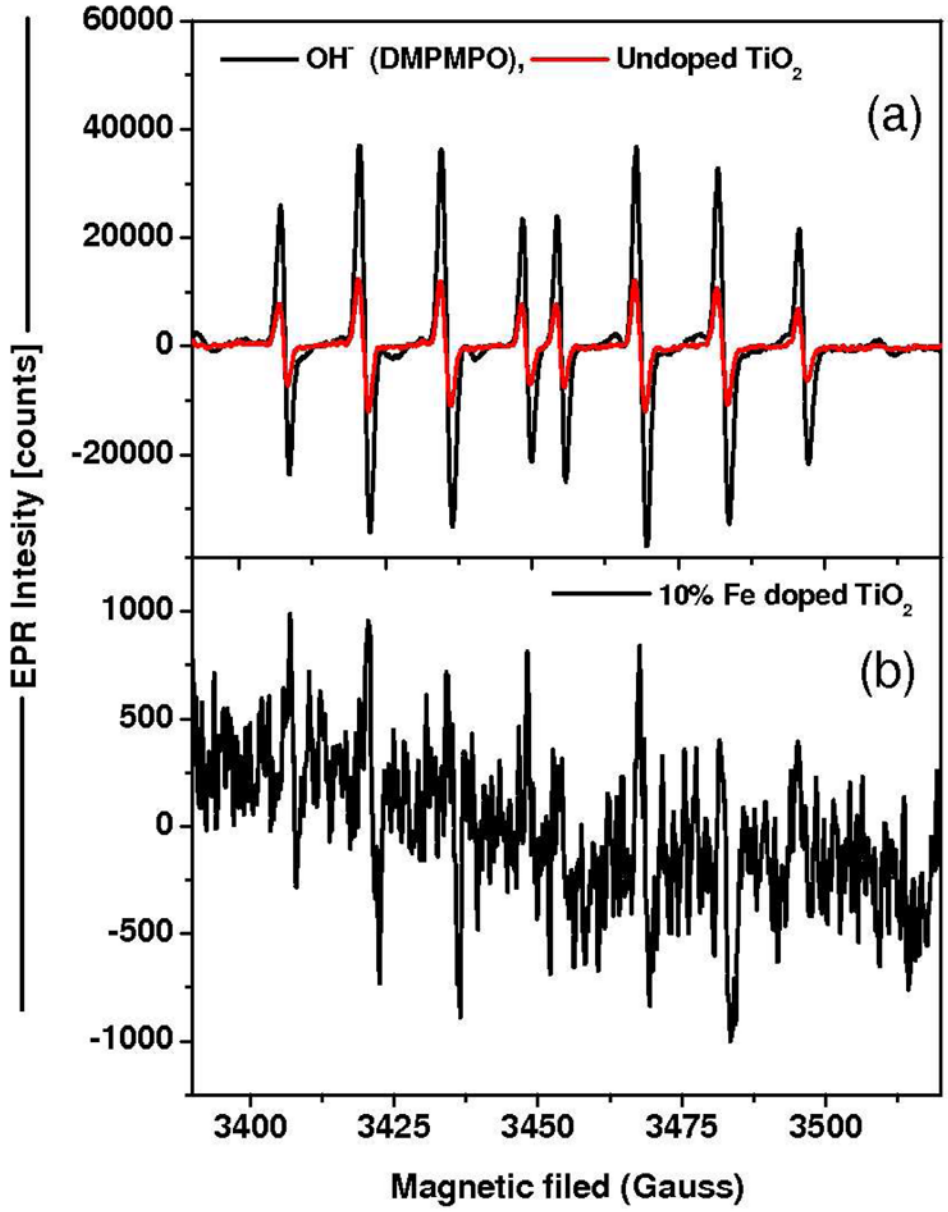

Figure 4.

EPR spectrum of pure and 10% Fe doped TiO_2. The EPR spectrum of spin adduct from HO• radical generated by Fenton reaction was used to compare the spectral features of TiO_2 activation. The EPR spectrum of the spin adducts was recorded 1 min after the addition of ferrous sulfate. The peak intensity from HO• radicals was drastically reduced in Fe doped TiO_2 NPs compared to pure TiO_2 under near visible light illumination.

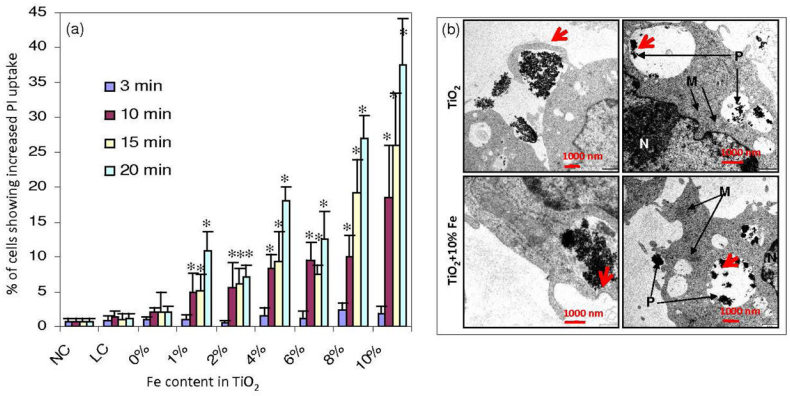

Figure 5.

Light energy dependent cell death upon exposure of nanoparticle treated RAW 264.7 cells to visible light and uptake of nanoparticles by RAW 264.7 cells. (a) The RAW 264.7 cells exposed to near-visible light after treatment with nanoparticles showed increasing percentage of cell death along with increasing light energy and Fe content. (b) TEM micrographs of RAW 264.7 cells treated with nanoparticles. The uptake of TiO_2 (upper panel) and Fe doped TiO_2 (lower panel) shows the closing of phagocytic appendages (arrows in the left panel images) in the process of engulfing the agglomerated nanoparticles. The arrows in the right panel images show the distribution of engulfed nanoparticles in phagosome compartments. NC -negative control, LC- light control. P- nanoparticle, M- mitochondria, N- nucleus. * statistically different from NC and LC $p \leq 0.05$.

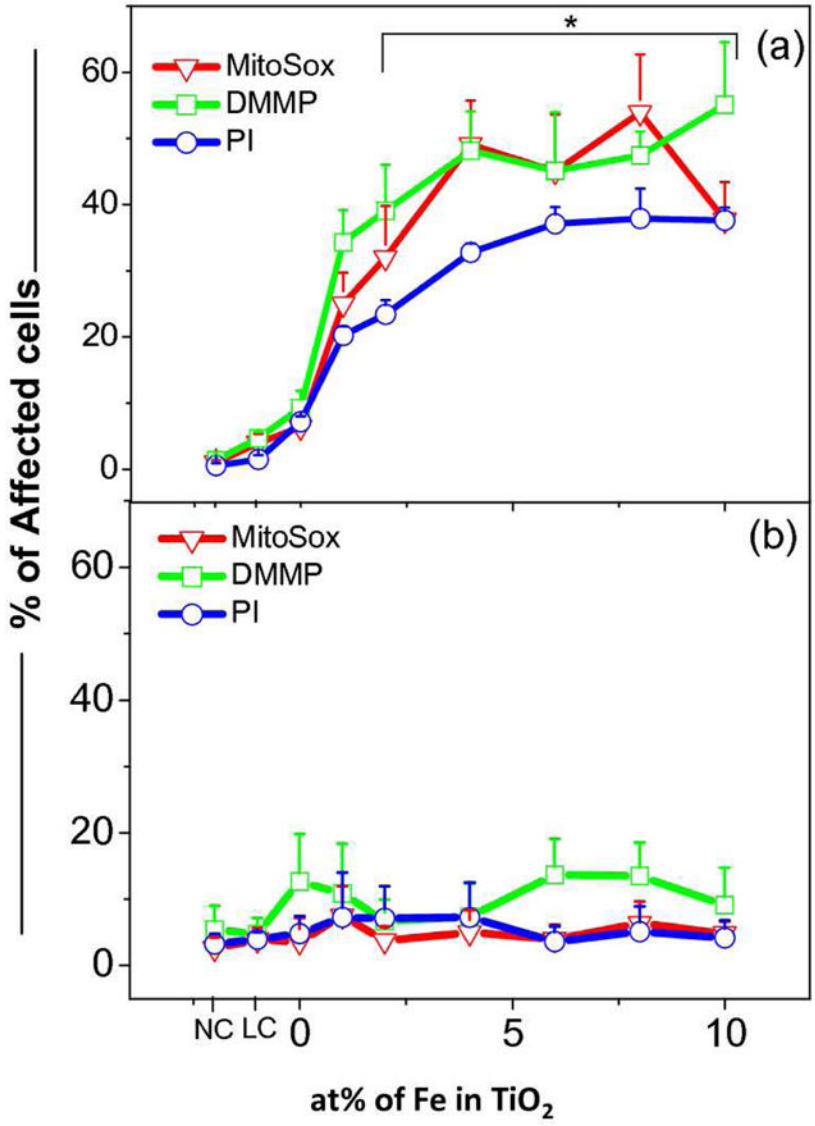

Figure 6.

Exposure of cells treated with nanoparticles to near-visible light illumination induced oxidative stress depended cytotoxicity in RAW 264.7. (a) RAW 264.7 cells treated with nanoparticle in CDMEM media for 24 hrs were washed and added with PBS. These cells were exposed to near-visible illumination for 20 mins. The medium was immediately replaced with CDMEM after illumination and incubated for 3 hrs followed by addition of fluorescence probes to assay for cytotoxicity responses such as, mitochondrial superoxide generation (MitoSox), decrease in mitochondrial membrane potential (DMMP) with respect to fluorescence dye (JC1), and loss of cell viability (PI uptake). (b) RAW 264.7 cells exposed to NPs as detailed above were treated with 100 μM of N-acetyl cysteine (NAC) three hours prior to near-visible light exposure and assessed for different cytotoxicity parameters as detailed above. NC-negative control, LC - light control. * statistically different from NC and LC $p \leq 0.05$

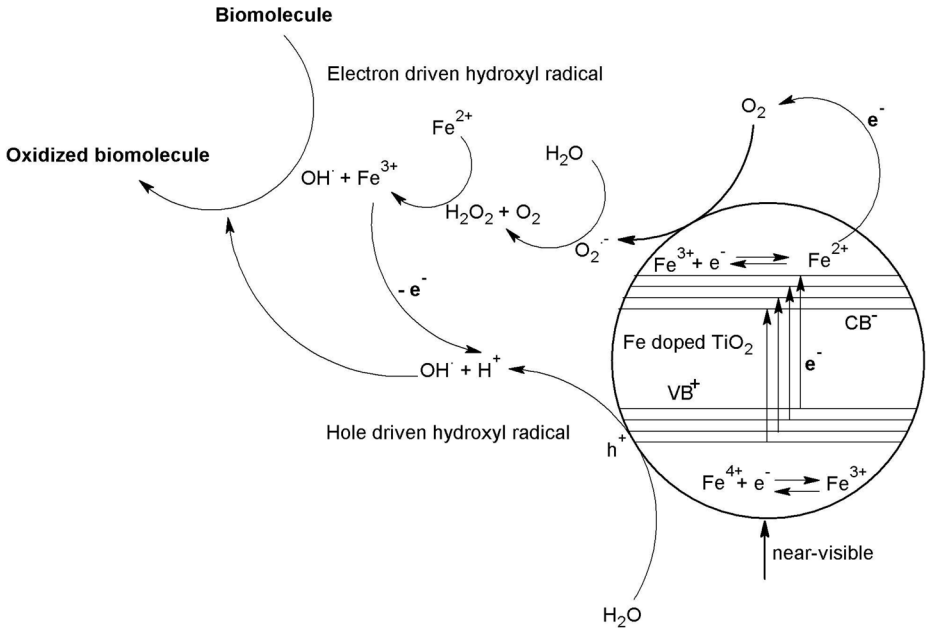

Figure 7.
The oxidation of biomolecules due to light induced ROS in the Fe doped TiO_2 nanoparticles